RESEARCH ARTICLE

Sensitivity of an asymmetric 3D diffuser to vortex-generator induced inlet condition perturbations

S. Grundmann · E. L. Sayles · Christopher J. Elkins ·
J. K. Eaton

Abstract Modifications of the turbulent separated flow in an asymmetric three-dimensional diffuser due to inlet condition perturbations were investigated using conventional static pressure measurements and velocity data acquired using magnetic resonance velocimetry (MRV). Previous experiments and simulations revealed a strong sensitivity of the diffuser performance to weak secondary flows in the inlet. The present, more detailed experiments were conducted to obtain a better understanding of this sensitivity. Pressure data were acquired in an airflow apparatus at an inlet Reynolds number of 10,000. The diffuser pressure recovery was strongly affected by a pair of longitudinal vortices injected along one wall of the inlet channel using either dielectric barrier discharge plasma actuators or conventional half-delta wing vortex generators. MRV measurements were obtained in a water flow apparatus at matched Reynolds number for two different cases with passive vortex generators. The first case had a pair of counter-rotating longitudinal vortices embedded in the boundary layer near the center of the expanding wall of the diffuser such that the flow on the outsides of the vortices was directed toward the wall. The MRV data showed that the three-dimensional separation bubble initially grew much slower causing a rapid early reduction in the core flow velocity and a consequent reduction of total pressure losses due to turbulent mixing. This produced a 13% increase in the overall pressure recovery. For the second case, the vortices rotated in the opposite sense, and the image vortices pushed them into the corners. This led to a very rapid initial growth of the separation bubble and formation of strong swirl at the diffuser exit. These changes resulted in a 17% reduction in the overall pressure recovery for this case. The results emphasize the extreme sensitivity of 3D separated flows to weak perturbations.

1 Introduction

Adverse pressure gradient flows which include separation from a smooth wall have long been known to offer a major challenge to turbulence modeling, particularly for internal flows where there is a strong coupling between the rapidly growing turbulent boundary layers on the bounding walls and the core flow (Klein 1981). One problem is that the boundary layer turbulence does not satisfy equilibrium scaling laws used in simple turbulence models (Song and Eaton 2004). Reynolds stress transport models (Launder et al. 1975) do not assume local equilibrium, yet still often have difficulty in replicating experimental data for separated flows as shown below. Recent work suggests that the difficulty may lie more in the high sensitivity of separated internal flows to changes in the inlet conditions, which is the subject of this paper.

The asymmetric 3D diffuser flow study done by Cherry et al. (2008, 2009) was conceived as a rigorous test of turbulence modeling for internal separated flows. The experimental configurations allow the definition of all relevant boundary conditions simply and accurately enough to be computed precisely in numerical simulations. The low aspect ratio of the diffusers means that the full 3D configuration can be gridded without excessive use of computational resources and the fully developed rectangular

S. Grundmann (✉)
Center of Smart Interfaces, Technische Universität Darmstadt,
Flughafenstrasse 19, 64347 Griesheim, Germany
e-mail: grundmann@csi.tu-darmstadt.de

E. L. Sayles · C. J. Elkins · J. K. Eaton
Stanford University, Stanford, CA, USA

duct flow at the inlet allows computation of the diffuser inlet conditions at any fidelity needed. Furthermore, the three-component mean velocity field was measured throughout the entire diffuser flow. As a consequence, the Cherry 3D diffuser flows have become benchmark cases for many numerical simulations, including *ERCOFTAC Special Interest Group 15* (Jakirlić et al. 2010) and several independent groups (Abe and Ohtsuka 2010; Jakirlić et al. 2010; Schneider et al. 2010; Ohlsson et al. 2010). The numerical simulations show that it is crucial for the quality of the simulations to precisely reproduce the secondary flows that the experimental data exhibit at the inlet of the diffuser. These secondary flows are caused by Reynolds stress anisotropy in the corners of the inlet duct (Gessner and Jones 1965) and therefore cannot be reproduced by isotropic eddy viscosity models or other turbulence models that do not allow for the development of anisotropic turbulence. Large differences in the calculated size, shape, and position of the separation bubble were found when the inlet conditions were not correct.

The strong effect of the inlet condition prescription on the simulation results was surprising because the secondary flows were quite weak in the experiment. The measurements of Cherry et al. (2008) and the direct numerical simulations of Ohlsson et al. (2010) both show peak secondary velocities of less than 5% of the bulk average velocity in the channel. To further investigate this strong sensitivity to inlet secondary flows, Grundmann et al. (2010) perturbed the inlet flow using dielectric barrier discharge (DBD) plasma actuators mounted in the duct upstream of the diffuser. The actuators were oriented to generate spanwise flow in a thin layer of fluid adjacent to one wall of the inlet duct which produced a pair of streamwise vortices that interacted with the separating boundary layer. Depending on whether the actuators were operated continuously or in a pulsed fashion, the diffuser's overall pressure recovery coefficient could be varied between $Cp = 0.5$–0.7. This 40% variation was accomplished without any addition of streamwise momentum, corroborating earlier evidence of the extreme sensitivity of this flow to inlet secondary flows. Measurements of the streamwise pressure distribution and the diffuser exit velocity distribution for a wide range of DBD actuator parameters indicated that the separation bubble geometry underwent major qualitative changes as the forcing was varied.

A significant advantage of the original experiment by Cherry et al. (2008) was the fact that it included 3 component mean velocity data throughout the entire diffuser flow that allowed complete assessment of the separation bubble geometry for the two different cases studied. These high resolution data were acquired using phase-contrast magnetic resonance velocimetry (MRV) using techniques described in Elkins et al. (2003) and Elkins and Alley (2007). While classical optical techniques such as particle image velocimetry (PIV) and laser Doppler anemometry require optical accessibility and acquire data only in two-dimensional planes or at single points, MRV is capable of measuring full 3D3C velocity fields at high resolution throughout the entire diffuser flow. In principle, similar data could be acquired using advanced 3D optical techniques like tomographic PIV, but this would require a very large effort in data acquisition and processing. By contrast, the entire mean velocity field in a new diffuser configuration can be fully documented in several hours of scanning using MRV. A disadvantage is that phase-contrast MRV techniques were developed for use in liquid flows, and therefore cannot be used to study the effects of DBD plasma actuators, which only operate in gas flows.

The goal of the present research was to acquire detailed 3D data to understand how longitudinal vortex structures produce such strong changes in the 3D diffuser pressure recovery. Prior to doing that, the perturbation study using DBD plasma actuators was extended by reversing the actuator configuration to produce secondary flows directed towards the channel centerline instead of towards the corners. Next, small passive vortex generators were mounted on one wall of the inlet duct in order to create a pair of streamwise vortices similar to the ones generated by the plasma actuators. Pressure distributions in the diffuser were measured for nine configurations involving different vortex generator sizes, positions, and orientations. Two configurations were selected for detailed study because they produced substantial differences in the pressure recovery, similar to the DBD plasma actuator experiments. The vortices of each pair were counter-rotating and the rotation direction was different between the two configurations. The impact of the two vortex generator pairs on the diffuser flow was examined in detail using three dimensional mean velocity data measured using MRV. This paper presents an overview and interpretation of the experimental results. The two 3D data sets are available from the authors.

2 Experimental procedure

The diffuser under investigation is the exact same diffuser as studied by Cherry et al. (2008) and Grundmann et al. (2010). The area ratio of the diffuser is 4.8 and the expansion takes place over a length of 150 mm, which corresponds to 15 inlet channel heights, denoted h in the following. The inlet channel has a rectangular cross-section measuring 10 by 33.3 mm. The outlet has a square cross-section of 40 by 40 mm. The bottom wall and one side wall are flat and the top wall and the other side wall are inclined at angles of 11.3° and 2.56°, respectively.

The diffuser is fed through a 600 mm-long development channel of the same cross-section as the inlet of the diffuser. As shown in Cherry et al. (2009) this channel is sufficiently long (120 channel half heights) to produce fully developed turbulent flow upstream of the diffuser inlet. This fully developed rectangular channel flow includes an asymmetric pair of counter-rotating longitudinal vortices in each corner generated by Reynolds stress anisotropy (Gessner and Jones 1965). Figure 1, used with permission from Cherry et al. shows high resolution MRV data for a cross-section located 1.3 channel heights upstream of the inlet of the diffuser. Streamwise and in-plane velocities are plotted, showing the secondary flows and the fully developed state of the flow entering the diffuser for the baseline case. The peak secondary velocities reported in Cherry et al. are approximately 3.5% of the bulk average streamwise velocity. Direct numerical simulations of the same inlet geometry were performed by Ohlsson et al. (2010). Their highly-resolved results show peak secondary flows in the same range and give the detailed geometry of the vortices. The simulations also confirmed that the channel flow reached a fully developed state approximately 15 channel heights upstream of the diffuser inlet. Cherry's turbulence measurements showed peak streamwise rms velocity on the channel centerline of approximately 6% of the bulk velocity, in agreement with data from 2D channel flow experiments.

A transition piece upstream of the development channel morphs the circular cross-section of the pipe from the air/water supply system to the rectangular cross-section. Three grids inside the transition piece prevent flow separation and provide a uniform mean flow. A second transition piece downstream of the diffuser morphs the square cross-section back to the circular. More details of the air supply system and the diffuser are described in Cherry et al. (2008) and Grundmann et al. (2010).

The plasma actuator experiments were conducted in air flow while the MRV experiments were conducted in water flow. The pressure distributions for both the plasma actuator cases and the passive vortex generator experiments were measured in air flow. In order to match the experiments in air and in water, the Reynolds number based on the bulk velocity and the inlet channel height was adjusted to the value of 10,000 in all cases.

The pressure distributions of the diffuser were measured using a Setra model 239 pressure transducer. The pressure taps were placed on the flat bottom wall on a line parallel to the flat side wall of the diffuser, intersecting the diffuser's spanwise midpoint at the outlet. The pressure recovery coefficient $c_p = \frac{P - P_{\text{ref}}}{\frac{1}{2}\rho u_{\text{bulk}}^2}$ was calculated using the bulk velocity u_{bulk} ($u_{\text{bulk}} = 15.4$ m/s for $Re = 10$ k), determined from the flow rate, the density, and the cross-sectional area at the diffuser inlet. The uncertainty of the pressure coefficients, considering error propagation of the pressure and temperature measurements, calibration uncertainty, the uncertainty of the analog-digital converter, and the statistical uncertainty, was determined to be ± 0.013.

The plasma actuators were composed of two electrodes made of 0.08 mm-thick copper tape and a dielectric layer composed of five layers of polyimid tape of 0.068 mm thickness. A *Minipuls 2* generator from *GBS Elektronik* supplied the high voltage. The operating voltages of the plasma actuators in this work range from $E_{pl} = 5$ kV$_{\text{pp}}$ to $E_{pl} = 10$ kV$_{\text{pp}}$ at frequencies between $f_{pl} = 10$ kHz and $f_{pl} = 12.6$ kHz. The computer-generated control signal for the high-voltage generator allows the plasma to be turned on and off rapidly, creating the pulsed forcing used in this investigation. The performance of the plasma actuators at various operating conditions was quantified in a separate setup. The wall jet produced by a plasma actuator in quiescent air was measured using a pitot tube and a micromanometer. The momentum J was determined from the velocity profiles. The momentum was related to the momentum of the inlet flow of the diffuser using the expression: $C_\mu = \frac{Jl}{q_\infty S}$, where J is the calculated momentum of the wall jet, q_∞ is the total pressure of the inlet flow, l is the length of the plasma actuator and S is the cross-sectional area of the channel. The geometry and position of the plasma actuators are depicted in Fig. 2 and the plasma actuator performance is quantified in Table 1. Please note
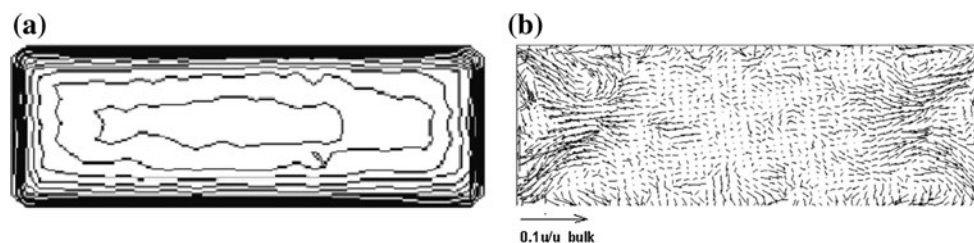

Fig. 1 High resolution MRV data from Cherry et al. The cross-section is located in the development channel, 1.3 channel heights upstream of the diffuser inlet. **a** Contour plot of streamwise velocity. The center contour has a value of 1.1 u/u_{bulk} and the contour interval is 0.1 u/u_{bulk}. **b** Vector plot of in-plane velocities
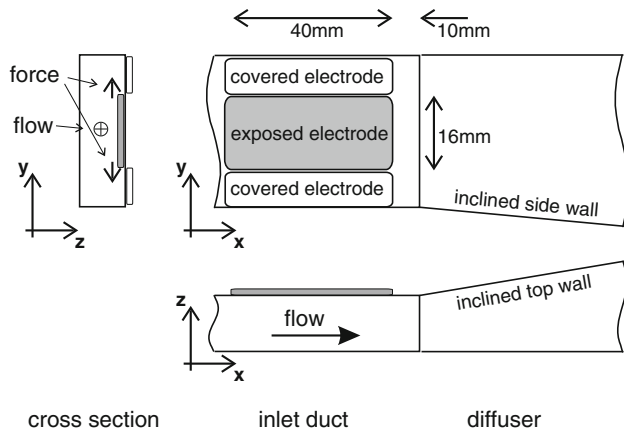
Fig. 2 Dimensions and position of the two DBD plasma actuators as used in this investigation

Fig. 3 Dimensions and position of the two vortex generator pairs as used in this investigation. The vortex generators are pitched at 22° in both cases

Table 1 Performance parameters of the plasma actuators used in this work

Voltage E_{pl} [kV$_{pp}$]	5	6	9	10
Frequency f_{pl} [kHz]	12.6	10.7	10.3	10.0
Momentum J [10^{-2} N/m]	0.07	1.06	1.80	2.66
Kinetic energy flux K [10^{-2} W/m]	0.023	1.38	2.87	4.83
Momentum Coefficient 10^{-2} C_μ	0.13	1.86	3.15	4.65
Dissipated power P [W/m]	17	52	78	114

The momentum coefficient has been calculated using an actuator length of 80 mm. All values correspond to continuously operated actuators. The kinetic energy flux at the inlet is 0.73 W

that the electrode arrangement of the plasma actuators as used in this investigation is the opposite of the arrangement in Grundmann et al. 2010. The forcing direction in this investigation is towards the center of the inlet channel.

Pressure data were acquired for nine different vortex generator configurations. Two configurations were chosen because they closely mimic the effects of the plasma actuators on the diffuser's pressure distribution. One set of vortex generators produces a degraded pressure recovery in comparison to the baseline case while the other improves pressure recovery. The details of the geometry of the vortex generators chosen for detailed study are depicted in Fig. 3. The vortex generators were made of 0.3 mm thick brass sheet metal and were mounted inside a flange that was inserted between the diffuser and the 600 mm long development channel. A template was used during vortex generator mounting to ensure that the pitch angle was accurate within 1°. The smaller vortex generators have a height normalized by the channel half width of 0.3, within the domain of low-profile vortex generators as defined by Lin (2002). The larger vortex generators were twice as high, but still significantly smaller than the channel half width.
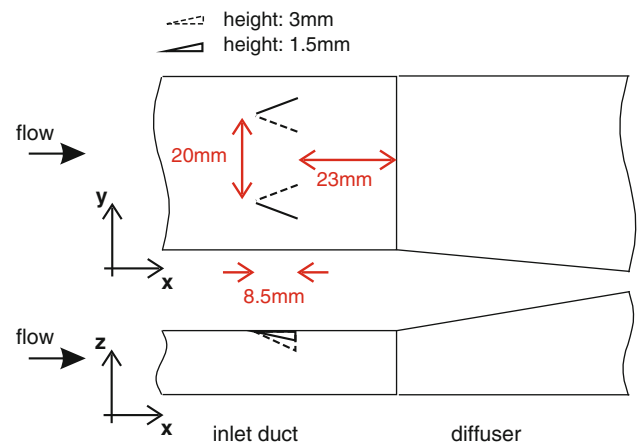
The magnetic resonance velocimetry (MRV) experiments were performed at the same Reynolds number as the air flow experiments. The working fluid was a 0.06 M solution of copper sulfate in deaerated water. The copper sulfate was added to the water to enhance signal strength and had minimal effect on the fluid properties. The Reynolds number of 10,000 based on the inlet channel height corresponded to a flowrate of 19.7 l/min and a bulk inlet velocity of 1 m/s. The diffuser was preceded and followed by the same development and exit components as for the air flow experiments. One-inch inner diameter flexible tubing formed the remainder of the closed loop and a centrifugal pump (Little Giant model no. TE-6MD-HC) fed the diffuser from a reservoir. The flowrate was measured with a Signet Scientific MK315.P90 paddle wheel flow meter. The MRV measurements were conducted at the Richard M. Lucas Center for Magnetic Resonance Spectroscopy and Imaging, located on the Stanford University campus. A standard transmitting/receiving head coil was placed in a 1.5 T GE whole body scanner which has a maximum gradient of 5 G/cm and a slew rate of 15 G/cm/ms. Phase-contrast MRV scanning was used as described by Elkins et al. (2003). Data were collected in 64 sagittal slices with a resolution given by 1 mm^3 voxels. The field of view is 260 mm in the streamwise direction and 78 mm in the remaining cross-streamwise direction. Five sets of flow-on scans were bracketed by flow-off scans. The flow-off scans were averaged and subtracted from the averaged flow-on data. Uncertainty in the velocity data was estimated to be 6% of the measured value using the techniques described in Elkins and Alley (2007) considering both biases due to local field gradient non-uniformities and random errors due to signal noise related to turbulent dephasing and the small size of the measurement voxels. These random errors were the dominant uncertainty source. The streamwise velocity

was integrated across each cross-section of the apparatus and typically agreed with the known flowrate within approximately 1%.

3 Results

3.1 Pressure recovery

The actuators used by Grundmann et al. (2010) were oriented to produce forcing in the spanwise direction, towards the corners of the inlet channel. Several operating conditions were investigated which involved varying both the forcing magnitudes and the duty cycles of the actuators, creating pulsed forcing. The pressure recovery was considerably decreased when the actuators were operated continuously. An increased pressure recovery was achieved only with pulsed operation of the plasma actuators. In the present investigation, the forcing direction has been reversed. These inverted plasma actuators produce forces directed towards the center of the inlet channel. As a result, the pressure recovery also shows an inverted behavior.

Figure 4 shows the pressure recoveries for different operating conditions. Continuous forcing at large amplitudes (10 kV_{pp}) with the reversed actuators yields an improved pressure recovery when compared to the baseline case. Continuous forcing at very low amplitudes (5 kV_{pp}) decreases the pressure recovery, which is again in contrast to the forcing towards the corners of the channel. Finally, pulsed forcing with a 40% duty cycle and a frequency of $f_{mod} = 50$ Hz strongly decreases the pressure recovery as compared to the baseline case. This last result is opposite of the case with forcing directed towards the corners of the
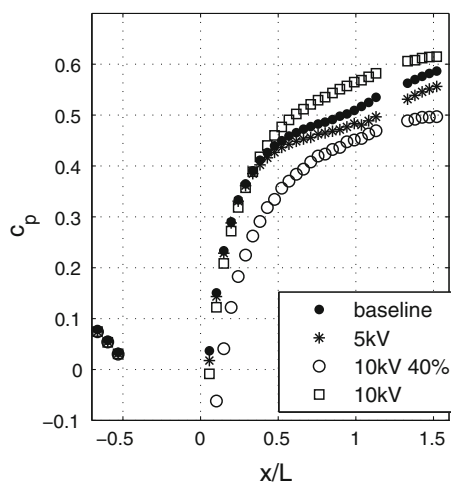
channel, which produced a large improvement in the pressure recovery.

The results obtained with the inverted plasma actuator forcing showed that substantial pressure recovery improvements of this diffuser can not only be obtained with pulsed forcing but also with continuously generated vortices, given that the position and rotation direction are chosen carefully. Depending on these parameters, it is possible to either decrease or increase the pressure recovery of the diffuser, without the pulsed generation of vortices. These findings motivated the design of the two pairs of passive vortex generators shown in Fig. 3. One configuration yields an improved pressure recovery and the other degrades the performance of the diffuser. Unlike the previously used plasma actuators, these passive devices can easily be applied in a water flow and magnetic resonance velocimetry can therefore be used to measure the full 3D3C velocity fields of the two different cases.

The pressure recovery along the diffuser obtained using the two different vortex-generator pairs is plotted in Fig. 5. The vortex generator pair that improves the pressure recovery was named VG1 and the pair that decreases the pressure recovery was named VG2. The two cases are clearly different in the development of the separation throughout the expansion of the diffuser. VG1, with the improved pressure recovery, matches the pressure recovery of the baseline case throughout the first 25% of the diffuser length. This indicates that the separation bubble is not much larger or smaller than the one in the baseline case. Downstream of the position $X/L = 0.5$, the two cases diverge and the baseline case begins to flatten, which indicates a sudden growth of the separation bubble. The VG1 case does not show this flattening and continues the growth of the static pressure in a
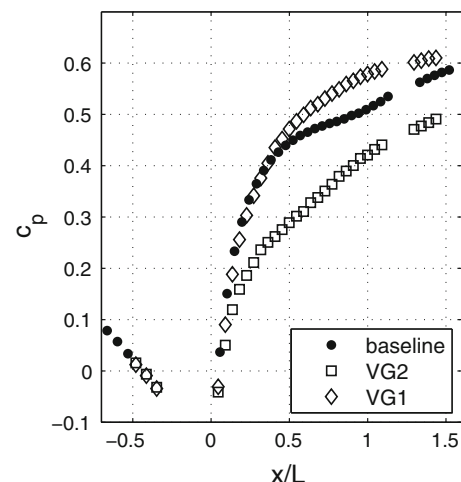

Fig. 4 Pressure recovery coefficient for reversed plasma forcing (towards the center). 40% means 40% duty cycle of the actuation. Other cases forced continuously

Fig. 5 Pressure recovery coefficient for the two vortex generator pairs and the baseline case

smooth curve. The pressure recovery for the VG2 case, on the other hand, stays far below the baseline and VG1 cases immediately after the beginning of the expansion. The differences in pressure between this and the other cases become even larger farther downstream. The very low pressure recovery within the first few centimeters of the diffuser length indicates the early development of a large separation bubble.

3.2 3D velocity data

The three-dimensional velocity data provide a means for understanding how the introduced vortices interact with the flow and the separation bubble, and how the resulting pressure recovery develops. Velocity data in the upstream channel for the two vortex generator cases are shown in Figs. 6 and 7. These cross-sections are located 2.5 channel heights upstream of the diffuser inlet for the VG1 case, and 1 channel height upstream of the diffuser inlet for the VG2 configuration. For both cases, the introduction of counterrotating pairs of longitudinal vortices has occurred upstream of the selected cross-sections. All of these cross-sections are plotted looking downstream, and the corner between the expanding walls is in the upper right.

The effect of the VG1 vortex generators on the mean streamwise velocity profile (taking the streamwise direction as the x-direction) is clearly visible in Fig. 6. Two counter rotating vortices carry the slow near-wall fluid into the center of the diffuser, between the two vortices, which creates a low speed streak that can clearly be seen in the contour plot of Fig. 6. The corresponding vector plot of the in-plane velocities shows the two vortices near the center of the upper wall. The vortices have diameters of about half the channel height. The in-plane velocities of the vortices

are on the order of 20% of the bulk velocity in the inlet channel, dominating any other three-dimensional motions in this plane. The measurement resolution isn't sufficient to fully resolve the cores of these vortices.

The vortices generated by the VG2 vortex generators are less intense and smaller in diameter as shown in Fig. 7. The vortices are closer to the corners for this case, and the image vortices associated with the upper channel wall drive them farther into the corners. Therefore, by the measurement plane, the two vortices are located very close to the corners. Their diameters are about one-third of the inlet channel height and the maximum in-plane velocity is of the order of 10% of the bulk velocity. Even these weak vortices dominate other secondary flows in the inlet channel. The vortices produce an accumulation of low speed fluid in the upper corners of the inlet channel.

The vortices emerging from the VG1 and VG2 vortex generators are visualized as iso-surfaces of constant x-vorticity $\omega = -0.05$ m/s^2 and $\omega = 0.05$ m/s^2 in Fig. 8 in blue and red, respectively. The VG1 case on the left with the highest pressure recovery shows two distinct and relatively large structures of equal size, shape and length. They stay almost symmetrically arranged in the center of the inlet, towards the beginning of the diffuser. The tubes of iso-surfaces with the same values for the VG2 case are clearly smaller in diameter than for the VG1 case, and the positions correspond to the ones shown in Fig. 7. In contrast to the VG1 case, the two VG2 vortices dissipate at different rates, which results in a difference between the lengths of the iso-surfaces. The structure that runs into the corner between the inclined walls, which is where the separation bubble begins, has only half the length of the other. This is caused by the strong shear stresses and turbulence that occur in the separated shear layer.
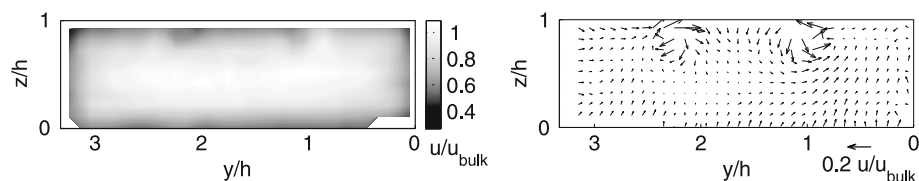

Fig. 6 Velocities in the inlet channel of the diffuser (x/h = −2.5) of the VG1 case. All plots are looking downstream with the corner between the two inclined walls in the *upper right*
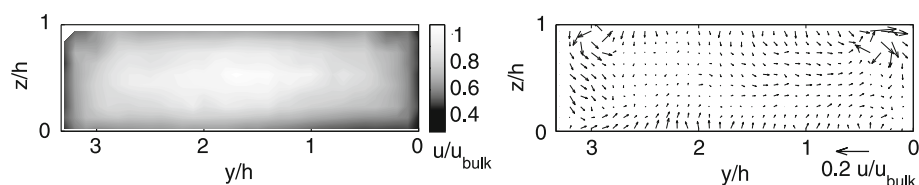

Fig. 7 Velocities in the inlet channel of the diffuser (x/h = −1) of the VG1 case. All plots are looking downstream with the corner between the two inclined walls in the *upper right*

Fig. 8 Iso-surfaces of x-vorticity $\omega = -0.05$ m/s^2 and $\omega = 0.05$ m/s^2. *Left* VG1, *right* VG2
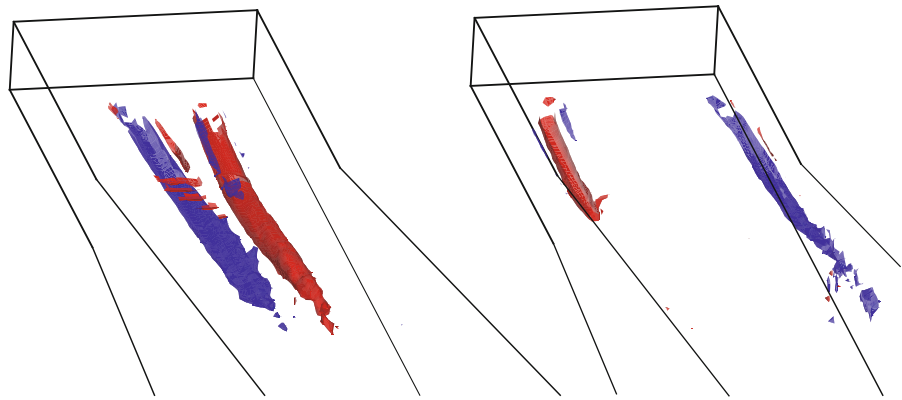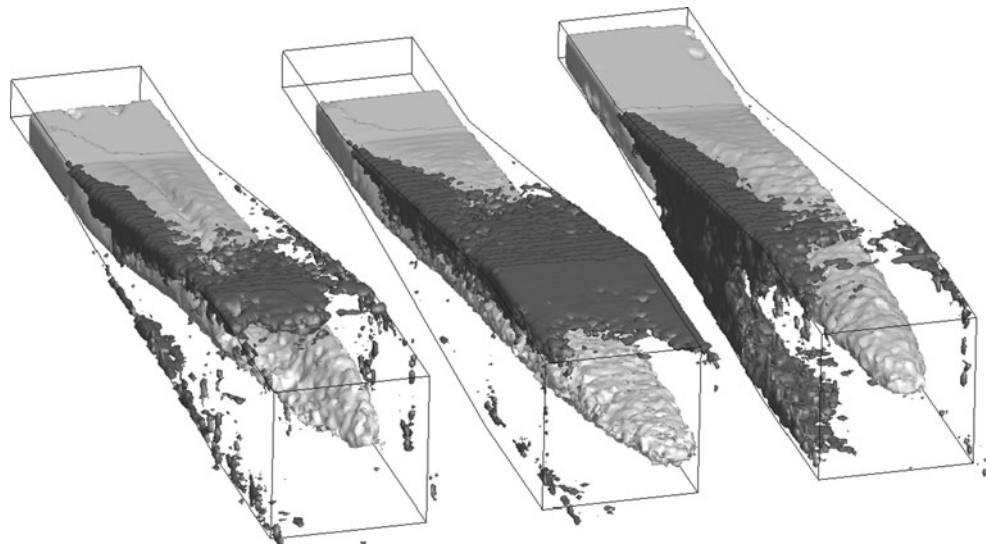

Fig. 9 Iso-surfaces of x-velocities $u/u_{bulk} = -0.01$ and 0.4. From *left* to *right* VG1, baseline case, VG2. The pressure recovery of the three cases decreases from *left* to *right*

The sizes of the separation bubbles of the three cases are illustrated in Fig. 9. The figure shows iso-surfaces of two different streamwise velocities, $u/u_{bulk} = -0.01$ and $u/u_{bulk} = 0.4$, dark gray and light gray, respectively. The pressure recovery of the three cases decreases from left to right. The iso-surface for a small negative velocity is used to illustrate the sizes, positions and shapes of the separation bubbles. The main flow is pushed towards the flat side wall away from the separated region in all three cases. The VG1 vortices show a clear impact on this iso-surface. It is deformed and has a dip, showing slower fluid in the center, that persists throughout the whole diffuser. It is obvious that the VG1 case on the left of Fig. 9 has the smallest separation bubble and therefore yields the highest pressure recovery. The position and shape of this separation bubble are similar to the characteristics of the bubble in the baseline case: the bubble begins in the corner between the two inclined walls and spreads along the whole width of the diffuser. However, the size of the VG1 separation bubble is much smaller. In addition to the main separation bubble, a small region of separated flow appears in the corner between the bottom wall and the inclined side wall. This is due to the increased positive pressure gradient that develops on the bottom wall, as compared to the baseline case with the larger main separation bubble. The VG2 case shows a completely different separation bubble. The bubble's position has switched from the top wall to the inclined side wall. It initially starts in the same corner but instead of spreading across the top wall, it spreads across the side wall much earlier in the expansion. The flow remains separated in the two corners bounding the inclined side wall farther downstream.

Figure 10 shows the fraction of the cross-sectional area occupied by reversed flow as a function of distance downstream of the diffuser inlet. The plots for the three cases are substantially different. The separation bubble in the VG1 case is the smallest throughout the whole diffuser. The VG1 curve follows the baseline case up to the position $x/L = 0.25$, just as the corresponding pressure recovery does. Starting from there the two curves diverge and the relative area of the reversed flow in the VG1 case remains more or less constant while the separation bubble of the
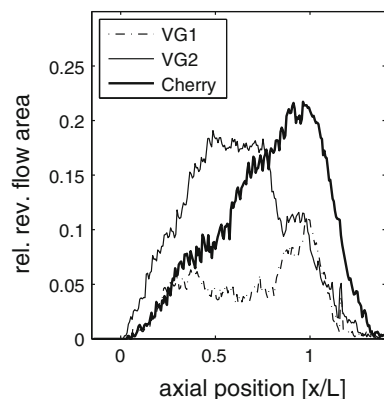
Fig. 10 Relative reversed flow area

baseline case grows continuously, almost linearly, up to $x/L = 1$. VG1 also shows a local maximum of the separation bubble size around $x/L = 1$. The growth of the separated zone of the VG2 case is different: the growth is much faster than in the baseline case and is almost linear. Even though this case has the lowest pressure recovery, the maximum size of the separation bubble is smaller when compared to the baseline case. However, the much faster growing separation zone yields higher losses due to the reduced effective cross-sectional area fairly early in the diffuser. The higher velocities produce higher losses due to friction and shear.

A second reason for VG2's lower pressure recovery despite showing a smaller separation zone can be found by looking at the in-plane velocities downstream of the diffuser. Figure 11 shows contour plots of the in-plane velocities at the end of the expansion at $x/L = 1$ for all three cases. While the baseline case (Fig. 11a) and the VG1 case (Fig. 11b) do not have any significant in-plane velocities at that position, the case with the worst pressure recovery, VG2, shows relatively strong in-plane motions in the center of the cross-section (Fig. 11c). The in-plane velocities are of the order of one-half of the bulk velocity calculated using the cross-sectional area at this downstream position.

A closer look at the vector plots of the in-plane velocities shows a very clear rotational movement for the VG2 case (Fig. 12c). A vortex core can be identified at the coordinates $y/h = 1$ and $z/h = 1$, which is the corner between the flat bottom wall and the expanding side wall. The corresponding vector plots of the baseline case 12(a) and the VG1 case 12(b) do not show such a clear and concentrated rotational movement of the fluid. The occurrence of such large scale vortical structures motivates the calculation of the swirl number S for this diffuser flow for all three cases. The swirl number was defined as follows:

$$S = \frac{G_\omega}{R G_x} \tag{1}$$

$$G_\omega = \rho \int_A v_x v_\omega r \, dA \tag{2}$$

$$G_x = \rho \int_A V_x^2 \, dA \tag{3}$$

where R is the hydraulic radius defined as $R = 2A/l$ with A as the cross-sectional area and l as its perimeter. v_x is the streamwise velocity component and v_ω is the circumferential velocity component, referred to the center of the cross-section at each downstream position of the diffuser. r is the distance to the center of the cross-section.

The swirl number determined for all three cases is plotted in Fig. 13. All cases show negative values along the x-axis, caused by the displacement effect of the separation bubble that starts in one corner and grows in size. The baseline case has the lowest values of the swirl number along the whole diffuser. The swirl is reduced to a minimum at the end of the expansion ($x/L = 1$) and increases again as a result of the asymmetric transition piece that morphs the square-shaped cross-section of the diffuser outlet to the circular pipe connection of the fluid-supply system. Figure 12a shows the corresponding vectors of the in-plane velocities of the baseline case. No clear in-plane rotation can be identified.

The swirl of the VG1 case is a little stronger than the maximum of the baseline case, but it remains almost constant throughout the diffuser. The corresponding velocity vectors in Fig. 12b reveal a weak vortex with its center located at $y/h = 1.5$ and $z/h = 3$.

The VG2 case shows the strongest swirl (Fig. 13) and the quickest growth of the separation bubble (Fig. 10). The vortex shown in Fig. 8 that runs towards the separation bubble is pushed sideways along the top wall out of the corner by the reversed flow inside the separated region. Simultaneously its image vortex pushes it back towards the corner making it stay attached right to the separation bubble. Its own rotation induces a downward motion inside the separated region, which promotes the growth of the separation bubble. This vortex is in a region of strong shear stresses and turbulence, near the top wall and the reversed flow, and dissipates faster than the other vortex. However, the faster growth of the separated region and its shape induce a rotational movement in the diffuser flow leading to the strongest swirl of all three cases. The swirl is still relatively strong at ($x/L = 1$), as Fig. 12c clearly shows.

Figure 13 offers an explanation as to why the pressure recovery of VG2 is the lowest despite having a smaller reversed flow area relative to the baseline case. The VG2 case has the strongest swirl of all three cases throughout the whole diffuser. Some of the kinetic energy is not converted into pressure but remains in a rotational movement of the diffuser flow.

Fig. 11 In-plane velocities $(v_y^2 + v_z^2)^{1/2}/u_{bulk}$ at the end of the expansion ($x/L = 1$). All plots are looking downstream with the corner between the two inclined walls in the *upper right*

(a) baseline case

(b) VG1

(c) VG2

4 Conclusions
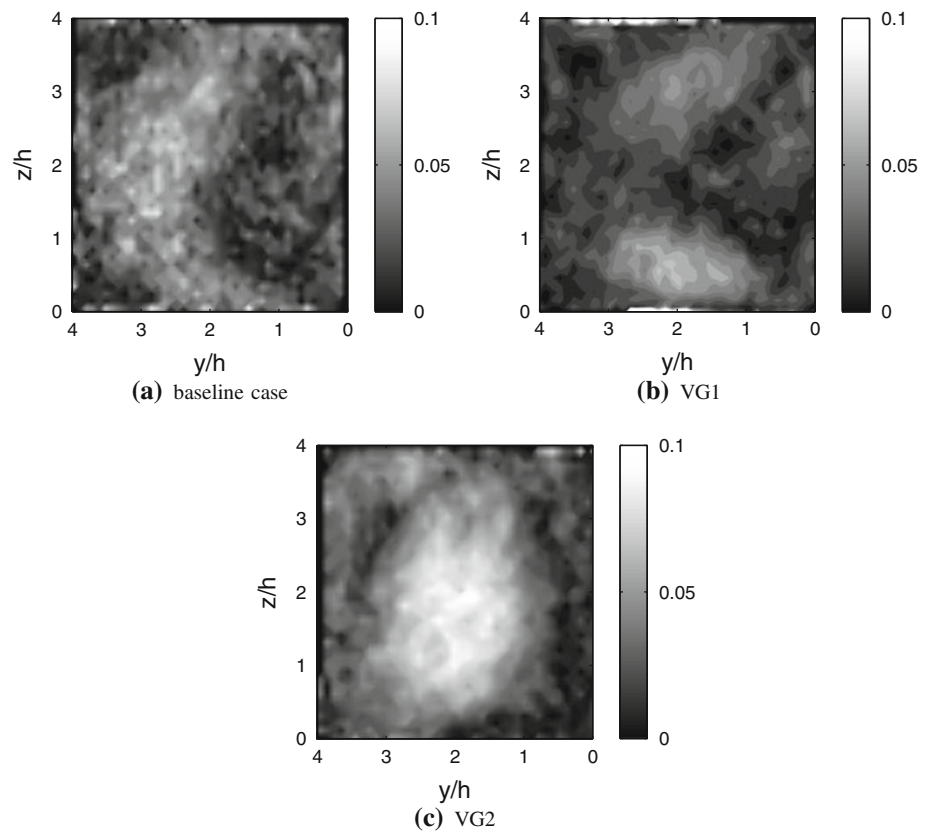
Another reason for the lower pressure recovery of VG2 is indicated by the stronger in-plane velocity in the outlet plane of the diffuser, shown in Fig. 11. VG2 exhibits the highest in-plane velocities at that position, indicating that the flow still is very much under development at that position. This is significantly different than the baseline case and the VG1 case. The in-plane velocity of VG2 at $x/L = 1$, which is mainly rotational, is of the order of one-third of the bulk velocity.

VG1 has the smallest separation bubble (Fig. 10), little swirl (Fig. 13) and the lowest in-plane velocities at the outlet (Fig. 12). Furthermore the two vortices remain antisymmetric as they move downstream (Fig. 8). It is obvious that this case must yield the highest pressure recovery.

4 Conclusions

Both the present work and previous studies have shown that the performance of three-dimensional stalled diffuser flows is extremely sensitive to weak upstream secondary flows produced by plasma actuators. Previous work on low-profile vortex generators reviewed by Lin (2002) showed that arrays of small vortices could significantly alter the flow distribution in S-shaped diffusers. The present

detailed velocity field measurements for the Cherry et al. diffuser with upstream vortex generators show that weak inlet vortices can produce complex changes in the separated flow and that the explanation for the changes to the pressure recovery may be more complicated than it was thought previously.

Vortices which are injected so they remain near the centerline of the expanding wall act to delay separation on that wall resulting in a smaller separation bubble. Typically, longitudinal vortices are thought to delay separation by increasing turbulent mixing. However, in this case, the mean flow directed toward the upper wall on the outside of each vortex appears to play an important role in preventing the corner separation from spreading across the entire wall of the diffuser. A key point is that the overall pressure recovery is improved in this case because the mainstream flow decelerates very rapidly in the upstream section of the diffuser, reducing the losses due to turbulent mixing once the separation bubble does form.

Vortices which are injected with the opposite sense move quickly into the diffuser corners where they interact with the secondary flows developed in the upstream channel. This leads to rapid growth of a separation bubble on the diffuser side wall, and the elimination of one of the vortices by rapid turbulent mixing. The surprising feature is that the overall pressure recovery is significantly reduced

Fig. 12 In-plane velocity vectors at the end of the expansion ($x/L = 1$). All plots are looking downstream with the corner between the two inclined walls in the *upper right*
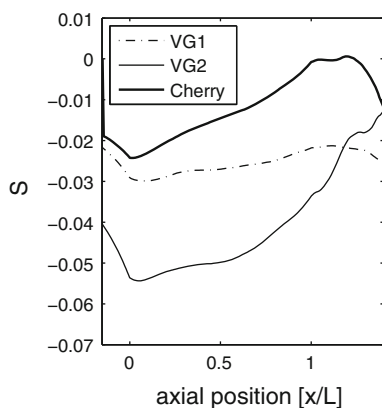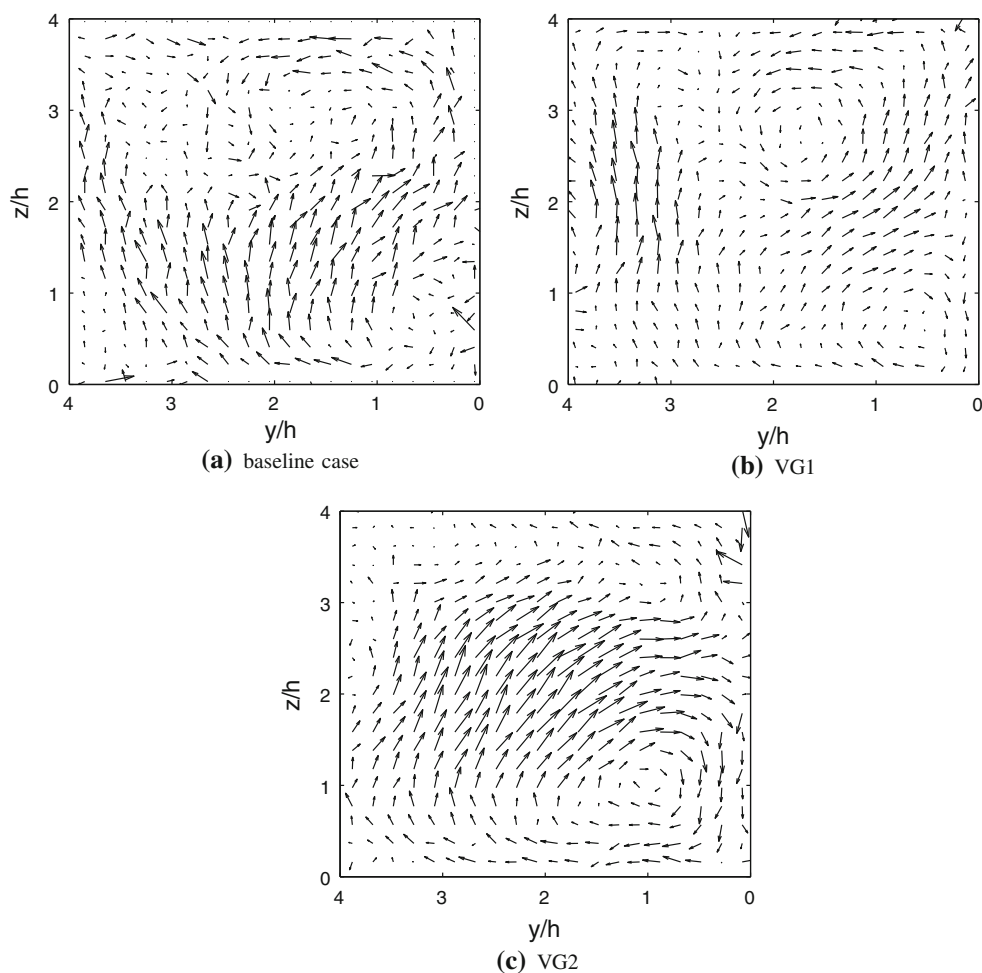

(a) baseline case

(b) VG1

(c) VG2

Fig. 13 Swirl number

even though the total size of the separation bubble is reduced. As opposed to case VG1, this case has very rapid early growth of the separation bubble. This keeps the mainstream velocity high resulting in strong losses in the separated shear layer. Also, the asymmetric effect of the vortices produces a strong secondary flow in the

diffuser that carries a significant fraction of the total energy in the outlet flow.

It will be interesting to see if modern CFD methodologies can capture these complicated effects. It is clear that the details of the upstream secondary flows play a critical role in controlling the separation bubble geometry. In the original baseline flow, accurate calculation of the secondary flows requires a model that can accurately represent the Reynolds stress anisotropy. Calculation of the secondary flows to sufficient detail may actually be simpler when they are forced by plasma actuators or delta wing vortex generators. The present authors are eager to collaborate with computer modelers to investigate these questions, and the full data sets are available for distribution.

References

Abe KI, Ohtsuka T (2010) An investigation of les and hybrid les/rans models for predicting 3-d diffuser flow. Int J Heat Fluid Flow, 31(5):833–844, 2010. Sixth international symposium on turbulence, heat and mass transfer, Rome, Italy, 14–18 September 2009—Turbulence, Heat and Mass Transfer 6

Cherry EM, Elkins CJ, Eaton JK (2008) Geometric sensitivity of three-dimensional separated flows. Int J Heat Fluid Flow 29(3):803–811

Cherry EM, Elkins CJ, Eaton JK (2009) Pressure measurements in a three-dimensional separated diffuser. Int J Heat Fluid Flow 30(1):1–2

Elkins CJ, Markl M, Pelc N, Eaton JK (2003) 4d magnetic resonance velocimetry for mean velocity measurements in complex turbulent flows. Exp Fluids 34:494–503

Elkins CJ, Alley M (2007) Magnetic resonance velocimetry: applications of magnetic resonance imaging in the measurement of fluid motion. Exp Fluids 43:823–858

Gessner FG, Jones JB (1965) On some aspects of fully-developed turbulent flow in rectangular channels. J Fluid Mech 23:689

Grundmann S, Sayles EL, Eaton JK (2010) Sensitivity of an asymmetric 3D diffuser to plasma-actuator induced inlet condition perturbations. Exp Fluids 50(1):217–231

Jakirlić S, Kadavelil G, Kornhaas M, Schäfer M, Sternel DC, Tropea C (2010) Numerical and physical aspects in LES and hybrid LES/RANS of turbulent flow separation in a 3-D diffuser. Int J Heat Fluid Flow 31:820–832

Jakirlić S, Kadavelil G, Sirbubalo E, von Terzi D, Breuer M, Borello D (2010) In: 14th ERCOFTAC SIG15 workshop on turbulence modelling: turbulent flow separation in a 3-D diffuser. ERCOFTAC Bulletin, 82

Klein A (1981) Review—effect of inlet conditions on conical diffuser performance. J Fluid Eng 103:250–269

Launder BE, Reece GJ, Rodi W (1975) Progress in the development of a Reynolds-stress turbulent closure. J Fluid Mech 68(3):537–566

Lin JC (2002) Review of research on low-profile vortexgenerators to control boundary-layer separation. Prog Aerosp Sci 38:389–420

Ohlsson J, Schlatter P, Fischer PF, Henningson DS (2010) Direct numerical simulation of separated flow in a three-dimensional diffuser. J Fluid Mech 650:307–318

Schneider H, von Terzi D, Bauer HJ, Rodi W (2010) Reliable and accurate prediction of three-dimensional separation in asymmetric diffusers using large-eddy simulation. J Fluid Eng 132(3):031101

Song S, Eaton JK (2004) Flow structures of a separating, reattaching, and recovering boundary layer for a large range of Reynolds number. Exp Fluids 36:642–653. doi:10.1007/s00348-003-0762-2